Numerical simulation of thermoacoustic heat pumping inside a compact cavity

Yann Fraigneau, Nicolas de Pinho Dias, Catherine Weisman, Diana Baltean-Carlès

16ème Congrès Français d'Acoustique
11-15 Avril 2022, Marseille

Numerical simulation of thermoacoustic heat pumping inside a compact cavity

Y. Fraigneau[a], N. de Pinho Dias[b], C. Weisman[a,b], and D. Baltean Carles[a,b]

[a]LISN, CNRS, Orsay, France
[b]Sorbonne Université, Institut Jean le Rond d'Alembert, 4 Place Jussieu, 75005 Paris, France

On s'intéresse à l'étude numérique du pompage de chaleur thermoacoustique le long d'un empilement de plaques (stack) placé dans une cavité compacte soumise à un écoulement oscillant. Les longueurs caractéristiques de la cavité sont petites devant la longueur d'onde associée à la fréquence d'oscillation. Les champs de vitesse et de pression sont contrôlés par deux sources oscillantes : une source principale (ou source de pression) qui pilote les phases de compression et de détente du fluide, et une source secondaire (ou source de vitesse) qui agit comme un déplaceur à l'intérieur de la cavité. La simulation numérique de l'écoulement est réalisée à l'aide d'un code résolvant les équations de Navier-Stokes discrétisées à l'ordre 2 en temps et en espace. Le domaine étant acoustiquement compact, un modèle numérique basé sur l'hypothèse de faible nombre de Mach est utilisé pour représenter les effets de compression et de détente du fluide se produisant au cours d'un cycle thermo-acoustique. Dans un souci de simplification, la configuration géométrique choisie est bidimensionnelle. Nous étudions l'influence de plusieurs paramètres liés à la géométrie et aux propriétés thermophysiques des plaques du stack, à la variation de pression acoustique, à la vitesse de déplacement du fluide ainsi que celle du déphasage entre les sources sur la différence de température moyenne obtenue en régime périodique. Les résultats sont comparés aux résultats expérimentaux de G. Poignand et al. (Acta Acustica United with Acustica, 2011) ainsi qu'aux relations analytiques proposées par G. Poignand en s'inspirant de la théorie linéaire de Rott.

1 Introduction

Thermoacoustic effect is a phenomenon of heat transport driven by acoustic oscillations. It occurs in the gas oscillating in the vicinity of a conducting solid, within viscous and thermal boundary layers. Thermoacoustic devices are used to generate either heat pumping for refrigerating purposes or mechanical work for engine operating purposes. The energy conversion takes place in a thermoacoustic core consisting of a stack of solid plates or a porous medium made of mesh grids or another geometry, placed between two heat exchangers. The thermoacoustic core is usually placed inside a closed resonator in which the gas is working at the fundamental resonant frequency associated with the geometry of the resonator [1]. In the last years efforts were made to reduce the dimensions of the systems. One solution was to eliminate the resonator and create the acoustic field needed in the thermoacoustic core with two acoustic sources inside a non resonant compact cavity [2, 3, 4]. Following this initial idea a compact thermoacoustic refrigerator prototype for automobile applications was designed and built [5]. The resulting TACOT prototype is a compact thermoacoustic refrigerator working under high mean pressure (40 bar) in which the acoustic field is created with two acoustic sources. The main driver acts as a pressure source and the second source is a loud-speaker acting as a velocity source. The thermoacoustic core is a regenerator (mesh of stainless steel screens) placed between heat exchangers. The overall geometry is coaxial with a peripheral channel allowing a feedback flow. The acoustic sources are working at the same frequency and their amplitudes and phases are tuned independently. The frequency is set so that the associated wavelength is much greater than the dimensions of the device. The pressure oscillations in time are almost spatially uniform and the phase between particle velocity oscillations and pressure oscillation are controlled through the phase between both acoustic sources. The TACOT prototype was designed using the numerical code DeltaEC, based on the linear theory of thermoacoustics (Rott's equations), widely used to design and compute thermoacoustic devices [6]. In thermaocoustic systems nonlinear phenomena such as jet streaming, end effects or natural convection are responsible for reducing the efficiency. Those phenomena are partially described or simply neglected in previous models and the first reported experiments on TACOT prototype showed some discrepancies with DeltaEC predictions [5]. Therefore a numerical model of the flow and heat transfer capable to describe such non linear phenomena could help understand their effects.

In the present work a numerical simulation of the flow and heat transfer in a compact simplified thermoacoustic heat pump is proposed. It consists in solving Navier Stokes equations under a low Mach number approximation (using the numerical solver SUNFLUIDH [7]). The use of this non linear model is justified by the compactness of the device with respect to the characteristic wavelength of the acoustic sources. The main objective of this study is to show the relevance of such an approach for the simulation of heat pumping in compact cavities. Providing a fine description of the flow and heat transfer, the present study will enable the analysis of non linear regimes as well as other factors such as gravity or streaming effects. Moreover, in the linear theory of thermoacoustics the main role of acoustic propagation and local pressure gradients is always emphasized. In the present approach, we point out that thermoacoustic effects can be correctly represented by coupling two mechanisms : a compression-relaxation cycle and an oscillating fluid motion. The former is related to a homogeneous thermodynamic pressure component whose time variation is governed by a first source acting as an "acoustic driver". The latter is sustained by a second source, the "oscillating fluid generator" that imposes a sinusoïdal time-variation of the flow rate. In the result section, we show that thermoacoustic heat pumping is correctly described with this model for different sets of parameters such as the stack thermal conductivity, the drive ratio, the stack mean velocity (or particle velocity amplitude), the relative phase between pressure oscillations and particle velocity oscillations. The numerical results are compared with analytical estimates and experimental results of G. Poignand [2, 4, 5].

2 Numerical Models

2.1 Governing equations in the low Mach number approach

As already mentioned, the dimensions of the prototype under study are much smaller than the wavelength associated with the oscillation frequency of the two sources. Therefore the whole prototype can be considered as acoustically compact. The characteristic Mach number M based on a characteristic velocity scale (for example the imposed velocity of the oscillating fluid generator) and the speed of sound is very small. Solving numerically the fully compressible Navier-Stokes equations is too time consuming. Using asymptotic expansions in powers of the Mach number, Navier-Stokes equations can be simplified [8]. The pressure term is split into two components : a first order thermodynamic pressure component P_{th} which is homogeneous in space and depends only on time, and a much smaller dynamic pressure component P_{dyn} of order M^2. The equations are then :

$$\frac{\partial \rho}{\partial t} + \vec{\nabla} \cdot (\vec{V}\rho) = 0, \tag{1}$$

$$\rho \left(\frac{\partial \vec{V}}{\partial t} + \vec{V} \cdot \vec{\nabla} \vec{V} \right) = -\vec{\nabla} P_{dyn} + \vec{\nabla} \cdot \tau + \vec{f}_V, \tag{2}$$

$$\rho c_p \left(\frac{\partial T}{\partial t} + \vec{V} \cdot \vec{\nabla} T \right) = \vec{\nabla} \cdot \kappa \vec{\nabla} T + \frac{dP_{th}}{dt}, \tag{3}$$

$$P_{th} = \rho \frac{R}{\mathcal{M}} T, \tag{4}$$

with ρ the fluid density, $\vec{V} = (U, V, W)^T$ the velocity field, τ the stress tensor, $\vec{f}_V$ the volume forces. T the temperature, c_p the specific heat at constant pressure, κ the thermal conductivity, R the gas constant and $\mathcal{M}$ the molecular mass of the fluid.

Since the pressure is split into two components a closure relation is required to determine together P_{th} and ρ : Assuming that the entire mass of fluid is known at any time in the domain Ω, P_{th} is obtained by integrating over the whole domain the state equation (4), yielding :

$$P_{th} = \frac{R}{\mathcal{M}} \frac{\int_\Omega \rho d\Omega}{\int_\Omega \frac{1}{T} d\Omega}, \tag{5}$$

The heat equation is solved in the solid parts of the stack, assuming the continuity of heat flux at fluid-solid interfaces.

2.2 Numerical methods

The governing equations are solved following a finite difference approach of second order in time and space. Convective/advective fluxes and conductive/viscous terms are discretized with a second order scheme on a staggered grid. The time scheme is based on a Crank-Nicholson method where the diffusive terms are implicit in order to increase the numerical stability of the method with respect to the time step, which is based on the CFL criterion only.

The dynamic pressure component is solved by means of an incremental projection method commonly used for the simulation of incompressible flows [9] and adapted for the low-Mach number approach. For that, the divergence-free constraint is replaced by the mass conservation constraint by using equation (1). The projection method also allows to update the velocity field estimated from the momentum equation (2) in such a way that mass conservation is satisfied. More information can be found in [10], for example. To sum up, this leads to a Poisson's equation of the form :

$$\nabla^2 \cdot \Psi = \frac{\nabla \cdot \left(\rho^{n+1} \vec{V}^* - \frac{\partial \rho^{n+1}}{\partial t} \right)}{\Delta t}, \tag{6}$$

where $\Psi = P_{dyn}^{n+1} - P_{dyn}^n$ is the time increment of pressure, the index n denotes the time iteration, $\vec{V}^*$ is the velocity field estimated from the momentum equation (2), ρ the mass density obtained from the state equation (4), $\frac{\partial \rho}{\partial t}$ its time derivative and Δt the numerical time step. In order to satisfy the mass conservation equation (1), the velocity field is updated as :

$$\vec{V}^{n+1} = \vec{V}^* - \frac{\Delta t}{\rho^{n+1}} \nabla \Psi, \tag{7}$$

The main steps of the algorithm used for the time advancement of physical quantities can be summarized as :

1. Solve equation (3) to update the temperature field.
2. Use the state equation in both forms (4) and (5) to obtain the thermodynamic pressure component P_{th} and the density ρ. This assumes the whole mass of fluid in the domain is known at each time step (see section 2.3.2 below).
3. Solve equation (2) to estimate the velocity field $\vec{V}^*$ (which does not satisfy mass conservation).
4. Use the projection method to compute the dynamic pressure component P_{dyn} and correct the velocity field in order to satisfy mass conservation.

2.3 Boundary conditions

2.3.1 Wall boundary conditions

Wall boundary conditions considered in this numerical study are classical. The usual impermeability and no-slip conditions ($\vec{V} = 0$ on the solid walls) are used for the velocity. Walls are considered as adiabatic (except for the stack plates) which implies to impose a zero normal derivative for temperature. Since velocity values are fixed, the projection method naturally imposes a zero normal derivative for the dynamic pressure component P_{dyn}.

2.3.2 Modeling the compression/relaxation cycle and the oscillating motion of the fluid

The experimental technology used to monitor the governing pressure variation and oscillating fluid motion consists in various acoustic sources, like pistons and

loudspeaker membranes. These complex elements are difficult to model in a CFD code. This would require specific methods managing moving objects in a fluid, like ALE or immersed body methods, as well as a finer mesh refinement in the zones of interest. As a consequence, numerical simulations would be particularly complex and time consuming. To overcome this difficulty, we have opted to model the acoustic sources by using oscillating flowrate inlets (see Figure 1). For each acoustic source, the boundary conditions are defined as :

$$Q_m(i) = \rho_0 U_i S_i \sin(2\pi f_0 t - \phi_i), \tag{8}$$

where $Q_m(i)$ is the mass flow rate at each inlet i with an amplitude $\rho_0 U_i S_i$ (reference values of fluid density, velocity and surface of the inlet i) and a time variation defined from the oscillation frequency of the device f_0 and the phase ϕ_i. This formulation ensures mass conservation over each thermoacoustic cycle and allows us to know the mass of fluid at any time. For others quantities (temperature, density, dynamic pressure component) a zero normal derivative is imposed.

For sake of clarity the inlets are reported in red color in the sketch of the computational domain (see Figure 1). The oscillating fluid generator (OFG) is constructed from two back-to-back inlets which have the same parameters ρ_0, U_{OFG}, S_G, ϕ_{OFG}. The OFG model therefore produces a zero mass balance at any time and plays a role in the fluid motion only. By considering the phase of the acoustic driver as a reference ($\phi_A = 0$) and the quadratic phase delay between the pressure and the acoustic driver velocity, the usual phase shift between velocity and pressure can be expressed as $\Phi_u - \Phi_p = \frac{\pi}{2} - \phi_{OFG} \pm m\pi$ (where m is an integer).

The drive ratio (i.e. the ratio between the amplitude of pressure oscillation and the mean pressure) and the velocity scale in the stack are directly related to the flow rates of the acoustic driver and the oscillating fluid generator.

3 Configuration setup

3.1 Description of the thermoacoustic device

In this section, we describe the 2D academic configuration used in our numerical simulations. It includes the main components of compact thermoacoustic refrigerators designed in laboratory experiments [3, 5] : an acoustic driver (AD) controling the compression and relaxation cycle, an oscillating fluid generator (OFG), a peripheral channel (PC) allowing circulating fluid and a stack of 16 solid plates along which is created the temperature gradient (see Figure 1). The geometry is cartesian and the computational domain is restricted to the upper part of the device by assuming a symmetrical behavior of the flow with respect to the median-plane. The main geometrical features of the device are summarized in Table 1.

The physical properties of the stack plates are chosen to be representative of materials commonly used. The mass density is fixed at $\rho_s = 2000$ kg.m^{-3} and the thermal conductivity is set to $\kappa_s = 0.2$ W.m^{-1}.K^{-1} (except in section 4.2 where different values of κ_s are considered). The specific heat capacity is however set to an artificially small value ($c_{ps} = 10$ J.K^{-1}.kg^{-1}). The objective is to shorten the transition time before reaching a converged time-average state of flow and heat transfer, and thus reduce the CPU time. The value of c_{ps} has a negligible impact on the final temperature gradient in the stack.

Domain size	$1.42\ 10^{-1}$m $\times 2.80\ 10^{-2}$ m
Stack plate size	$5.00\ 10^{-2}$m $\times 1.28\ 10^{-3}$ m
distance between plates	$1.28\ 10^{-3}$ m
Stack area height	$2.11\ 10^{-2}$ m
Distance AD-OFG	$1.16\ 10^{-1}$ m
Distance AD-stack	$8.60\ 10^{-2}$ m
AD height	$1.54\ 10^{-2}$ m
OFG height	$2.11\ 10^{-2}$ m
Pheripheral channel height	$5.60\ 10^{-3}$ m

Tableau 1 – Geometrical features of the thermocoustic device defined in the half-domain.

The fluid is a gas mixture composed of 30% argon and 70% helium as in the TACOT experiments [5]. This choice is made in order to verify the ability of the numerical model to supply a high temperature gradient of the same order of magnitude as those obtained with the experimental prototype [5]. The perfect gas state law is considered with constant physical properties. The specific heat capacity, thermal conductivity and dynamic viscosity are set to $c_p = 1404.97$ J.K^{-1}.kg^{-1}, $\kappa = 8.56\ 10^{-2}$ W.m^{-1}.K^{-1} and $\mu = 2.11\ 10^{-5}$ kg.m^{-1}.s^{-1} respectively.

The frequency of the acoustic driver and the oscillating fluid generator is fixed at $f_0 = 50$ Hz. By considering a reference temperature of $T_0 = 298$ K and mass density of $\rho_0 = 0.597$ kg.m^{-3} , the thicknesses of the dynamic and thermal boundary layers along the stack plates are estimated to be $\delta_\nu = 4.75\ 10^{-4}$ m and $\delta_h = 8.07\ 10^{-4}$ m respectively.

3.2 Numerical parameters

The computational domain is discretized according to a cartesian grid 384×320 in the longitudinal (x) and the normal (y) directions respectively (with respect to the stack plates orientation). In the normal direction, the cell size distribution is regular over the stack area. There are 16 cells across the plate thickness as well as across the fluid interspace between plates, the resulting cell size being $\Delta y = 8\ 10^{-5}$ m. This ensures a correct spatial resolution of the boundary layers.

In the longitudinal direction, the cell size varies following a specific distribution law so that the minimum values are positioned nearby the stack ends ($\Delta x_{min} = 2.5\ 10^{-4}$ m).

The time step is fixed at $\Delta t = 2\ 10^{-5}$ s. This choice ensures the CFL criterion is satified (maximum value is about 0.5) and each period of the thermoacoustic cycle is exactly described with 1000 time steps.

Initially the fluid is at rest. Pressure and temperature are set to $P_0 = 10^5$ Pa and $T_0 = 298$ K and the mass density is

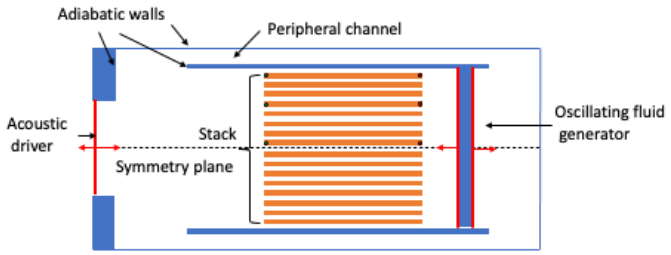

FIGURE 1 – Sketch of the 2D TACOT configuration. The computational domain is restricted to the upper part above the symmetry plane. Circle tags show probe locations used for recording time series of temperature.

equal to $\rho_0 = 0.597$ kg.m^{-3}. Several numerical studies are presented in the next section. For each case, the computation is performed until the time-average heat flux between the fluid and the stack is quasi-converged. The time-average heat flux is computed over a range of 100 thermoacoustic cycles.

4 Numerical results

The numerical results presented below are obtained for physical configurations adapted from experiments [3, 5] so that the operating mode mainly corresponds to the linear regime. The working gas and frequency were chosen to be the same as in the TACOT prototype [5] in order to obtain a thermoacoustic heat pumping effect large enough for industrial applications. However, the mean thermodynamic pressure was set to the atmospheric pressure in order to keep boundary layers large enough to be discretized without excessive numerical cost. Here the ratio between the half-distance between plates and the thermal boundary layer thickness is equal to 0.8 which means that the stack is neither quasi-adiabatic nor quasi-isothermal, but in between. Numerical simulations are then compared with analytical results obtained from linear theory [2] for various sets of parameters as well as with experimental measurements (by comparing normalized quantities when it is possible). Experimental points with a quasi-adiabatic stack (Exp 1) or quasi-isothermal regenerator (Exp 2) are considered since the numerical configuration configuration is in-between. In numerical simulations the operating case is described from the drive ratio, the stack velocity scale and the phase shift. The drive ratio is the commonly used parameter to characterize the acoustic operating regime : It is here defined with respect to the thermodynamic pressure component as :

$$Dr = \frac{P_{th}^{max} - P_{th}^{min}}{P_{th}^{max} + P_{th}^{min}}.$$

he stack velocity scale u_s is commonly defined as the mean velocity amplitude over the stack channels. It can be simply estimated as $u_s = \dfrac{U_{OFG}}{R_b}$ (the density variation in space being neglected as a first approximation), where U_{OFG} is the velocity amplitude of the OFG, and R_b is the stack blockage ratio (ratio between the solid part and entire stack volumes).

In the following discussion we start with a reference operating regime corresponding to a drive ratio equal to $Dr = 0.0236$, a velocity scale in the stack on the order of $u_s = 0.5$m.s^{-1} ($U_{OFG} = 0.25$ m.s^{-1} and $R_b = 0.5$), and a phase shift between the AD and the OFG equal to $\Phi_u - \Phi_p = 5\pi/6$. This is close to an optimal choice of parameters with respect to the final temperature difference between stack ends. All other input parameters are described in Section 3. In the following sections, only one input parameter will be varied at a time. Results focus on the temperature difference between stack ends, defined as the average of values computed for several stack plates.

4.1 Estimate of the temperature difference between stack ends

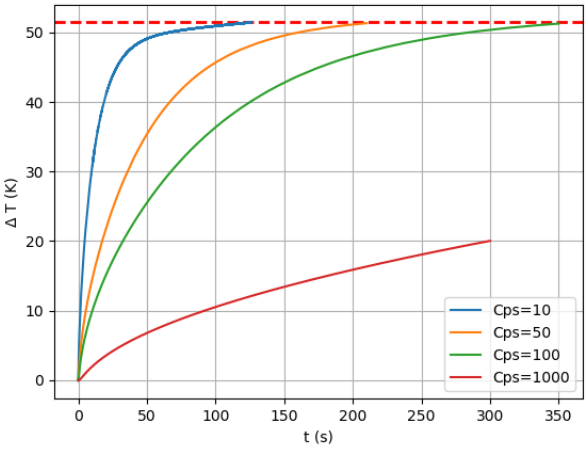

FIGURE 2 – Temperature difference between stack ends computed by numerical simulation for several values of c_{ps}.

The time evolution of the temperature difference ΔT is plotted in Figure 4.1 for several values of the stack plates' heat capacity c_{ps}. There is a transient phase before reaching an asymptotic regime giving the final value of $\Delta T = 51$ K, which, as expected, increases with the value of the heat capacity. However the final value of $\Delta T \approx 51.5$ K does not depend on the value of c_{ps} in the range $[10 - 100]$ J.K^{-1}.kg^{-1}. Rott's linear theory applied to this configuration developed in [2, 3] yields $\Delta T_{lin} = 48.7$ K with the present numerical input data set. The ΔT values are very close and of the same order of magnitude as those obtained in the TACOT prototype designed for industrial applications [5].

4.2 Influence of the stack thermal conductivity

Figure 3 shows the value of ΔT between stack ends for three values of the thermal conductivity κ_s of the solid stack plates. The solid line shows the prediction of the linear theory of thermoacoustics. The agreement is excellent. As expected, when κ_s is very large, ΔT becomes

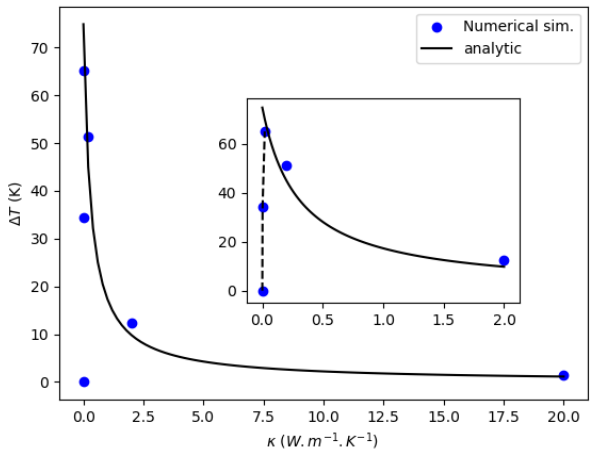

FIGURE 3 – Mean temperature difference ΔT between stack ends for 6 values of κ_s. Numerical results (blue dots), linear theory (solid line).

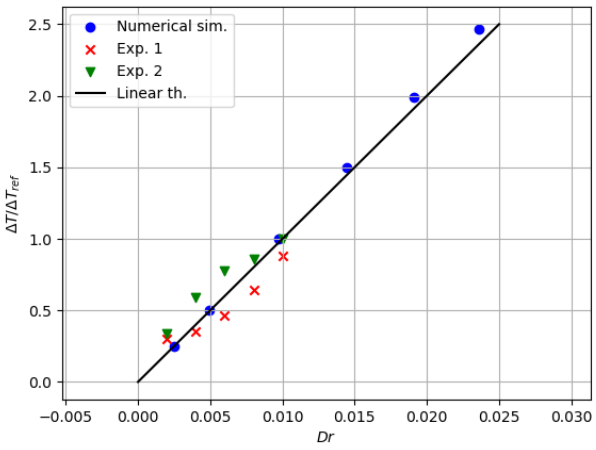

FIGURE 4 – Normalized mean temperature difference $\Delta T/\Delta T_{ref}$ between stack ends as a function of the Drive ratio Dr variation. numerical results (blue dots), linear theory (black solid line), Exp 1 (red crosses) and Exp 2 (green triangles) from [4].

negligible because of enhanced heat conduction in the solid : thermoacoustic heat pumping becomes ineffective. For $\kappa_s = 0$ (adiabatic stack) the thermoacoustic effect is canceled, as predicted by Swift [1]. Note that for very small (non-zero) values of κ_s the numerical prediction departs for the linear theory, suggesting that the evolution as $\kappa_s \to 0$ is sharp but continuous and that there is an optimum κ_s value for which ΔT is maximum.

4.3 Influence of the drive ratio

Figure 4 shows the variation of the normalized temperature difference along the stack with its maximum value as a function of the drive ratio. Numerical points are plotted as well as the linear theory prediction and experimental results from [4].

In order to compare our results with those of Poignand *et al.* [4], which are performed for very different physical conditions, the normalization scale ΔT_{ref} is chosen at $Dr = 0.01$. Both sets of experimental points (Exp 1) and (Exp 2) are shown on the figure, and the evolutions are consistent with the numerical simulation results which fall in between as expected, since in the numerical configuration the stack is neither fully adiabatic nor isothermal.

Very good agreement with the linear theory is observed (see Figure 4) up to $Dr = 0.015$. A slight but increasing discrepancy is observed for larger values of Dr, which is probably related to the onset of non linear effects.

4.4 Influence of the stack velocity-scale

Another important controlling parameter of the thermoacoustic heat pumping effect is the characteristic velocity scale within the stack.

In order to compare numerical, theoretical and experimental results, the stack velocity scale corresponding to each set is normalized with respect to its own optimum

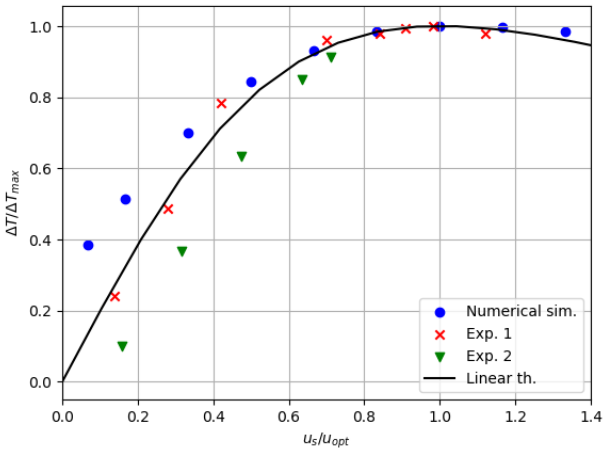

FIGURE 5 – Normalized mean temperature difference $\Delta T/\Delta T_{max}$ between stack ends as a function of the normalized stack velocity scale u_s/u_{opt}.

value u_{opt} providing the maximum value of the ΔT obtained in each case.

Figure 5 shows the evolution of ΔT between stack ends as a function of the normalized stack velocity scale $u_s^* = u_s/u_{opt}$. Again a similar behavior is observed in numerical or experimental results and in the linear theory. The value of ΔT increases with u_s^* approximately following the linear theory (up to u_s^* about 0.85), then reaches a plateau. The value of u_{opt} in the numerical configuration is approximately $u_{opt} = 0.58$ m.s^{-1}, while the linear theory yields $u_{opt} = 0.45$ m.s^{-1}. This discrepancy is not really meaningful due to the rather small sensitivity of ΔT around $u_s^* = 1$. Even

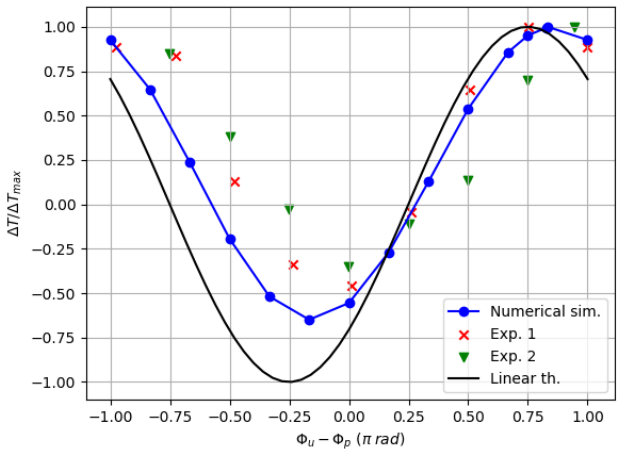

FIGURE 6 – Normalized mean temperature difference $\Delta T/\Delta T_{max}$ as a function of $\Phi_u - \Phi_p$.

though in the experiments, $u_{opt} = 1.43$ m.s^{-1} (Exp 1) and 1.26 m.s^{-1} (Exp 2), which are much higher values [4], the normalization allows to obtain analogous behavior for all these physically very different configurations.

4.5 Influence of the phase shift between velocity and pressure.

The influence of the phase shift between velocity and pressure is studied and results are plotted in Figure 6. Here again a similar evolution is observed in numerical simulations, experimental results and the linear theory. In the $[-\pi, 0]$ interval, numerical results are bounded by linear theory and experimental results, while in the $[0, \pi]$ interval all curves are in close agreement. Numerical simulations confirm the experiment results in that the phase shift has a major influence on the thermoacoustic heat pumping effect. Indeed it is possible to control the orientation of heat pumping (and invert ΔT between the stack ends) with the phase shift. The observed asymmetry of the curve (for example on extreme values) is probably correlated to the device geometry with respect to the stack middle cross-section. Note that the model deduced from the linear theory does not predict this asymmetry. The numerical optimum value $\Phi_u - \Phi_p = 5\pi/6$ is very close to the value found in the linear model ($3\pi/4$), and is bounded again by the experimental results reported in [4].

5 Conclusion

A numerical model based on a Low Mach number approximation was designed to simulate the thermoacoustic heat pumping effect inside a compact cavity consisting of an acoustic driver, an oscillating fluid generator and a stack of solid plates. In this fluid mechanics approach, the physical coupling between the oscillating fluid and homogeneous compression-relaxation cycles results in thermodynamic heat pumping along the stack plates with no account of acoustic propagation. The main characteristics of linear thermoacoustics as well as experimental measurements are recovered, at least in the linear regime. So far, the model was used to explore a wide range of input parameters in the linear regime. It is a promising tool to explore the non-linear regime and the influence of other physical effects such as gravity.

Acknowledgements

This research is financially supported by Agence Nationale de la Recherche (Projet ANR-17-CE06-0 0 07-01).

Références

[1] G. W. Swift, *Thermoacoustics : A unifying perspective for some engines and refrigerators*, J. Acoust. Soc. Am., Melville, NY (2002).

[2] G. Poignand, B. Lihoreau, P. Lotton, E. Gaviot , M. Bruneau and V. Gusev, Optimal acoustic fields in compact thermoacoustic refrigerators, *Applied Acoustics* **68**, 642–659 (2007).

[3] G. Poignand, P. Lotton, G. Penelet and M. Bruneau, Small Cavity Excitation to Achieve Optimal Performance, *Acta Acustica united with Acustica* **97**, 926 – 932 (2011).

[4] G. Poignand, A. Podkovskiy, G. Penelet, P. Lotton and M. Bruneau, Analysis of a Coaxial, Compact Thermoacoustic heat pump, *Acta Acust. United Ac.*, **99**, 898 – 904 (2013).

[5] I. A. Ramadan, H. Bailliet, G. Poignand, and D. Gardner, Design, manufacturing and testing of a compact thermoacoustic refrigerator. *Applied Thermal Engineering*, **189** 116705 (2021).

[6] B. Ward, J. Clark, and G. W. Swift, *Design Environment for Low-amplitude Thermoacoustic Energy Conversion (DeltaEC Version 6.2)*, Users Guide, (Los Alamos National Laboratory (2008). http ://www.lanl.gov/thermoacoustics/UsersGuide.pdf.

[7] Y. Fraigneau. $https : //sunfluidh.limsi.fr/sunfluidh : sunfluidh\_full\_documents$ (2013).

[8] S. Paolucci, *On the filtering of sound from the Navier-Stokes equations*, Report No. SAND82-8257, Sandia National Laboratories (1982).

[9] K. Goda, A multistep technique with implicit difference schemes for calculating two- or three-dimensional cavity flows, *Journal of Computational Physics*, **30**, 76-95 (1979).

[10] R. Knikker, A comparative study of high-order variable-property segregated algorithms for unsteady low Mach number flows,*Int. J. Numer. Meth. Fluids*, **66**, 403-427 (2011)